Measurement and Simulation of Laser Imprinting and Consequent Rayleigh-Taylor Growth

R. J. Taylor,[1] J. P. Dahlburg,[2] A. Iwase,[1] J. H. Gardner,[2] D. E. Fyfe,[2] and O. Willi[1]
[1]*Imperial College of Science, Technology and Medicine, London SW7 2BZ, United Kingdom*
[2]*LCP&FD, Naval Research Laboratory, Washington, D.C.*
(Received 2 June 1995; revised manuscript received 22 November 1995)

High-resolution, high-contrast images have been obtained of the imprint of laser nonuniformity and subsequent Rayleigh-Taylor (RT) growth in planar foils driven by coherent and temporally incoherent light. The experimental results are well reproduced by three-dimensional radiation transport hydrodynamics simulations. The role of hydrodynamic motion within the target from early time is highlighted, and a period of RT growth during which longer modes dominate is isolated.

PACS numbers: 52.40.Nk, 52.35.Py, 52.65.Kj

A severe limitation on the efficiency of a high-gain direct drive (DD) inertial confinement fusion (ICF) implosion is the extent of pellet disruption caused by Rayleigh-Taylor (RT) growth of imperfections at the pellet ablation surface. The RT instability is seeded by both pellet mass inhomogeneities and by nonuniformities in the incident laser beam during the low irradiance ($1 \times 10^{12} < I < 5 \times 10^{13}$ W/cm^2) "start-up" phase, which gives rise to ablation pressure nonuniformities that can imprint the target. Thermal smoothing [1] helps to ameliorate the imprint at later times, but at start-up the driving pressure profile matches that of the laser. Much research has been focused on improving the spatial uniformity of the drive irradiation through the introduction of spatial and/or temporal incoherence [2], although such techniques have been unable to produce entirely uniform profiles on relevant hydrodynamic time scales.

The irradiation nonuniformity generated by a high-power laser system is essentially random with a large small-scale ($\sim$10 μm) component, and fully two dimensional (2D). Imprinting of these nonuniformities on the ablation surface of solid targets has been qualitatively observed experimentally in a side-on configuration [3] using an imaging system operating in the extreme ultraviolet (XUV), although face-on radiography is required to obtain quantitative data suitable for comparison with analytical and numerical models. Previously, the only face-on techniques available have operated at x-ray energies ($h\nu \sim 1$–3 keV), with comparably low spatial resolution ($\sim$10 μm) [4]. We demonstrate here the first application of XUV imaging to face-on radiography, with sufficient temporal and spatial accuracy to quantify the effects of early-time laser imprint on ablatively accelerated plastic targets.

Experimental results thus obtained directly and successfully compare with those predicted by three-dimensional (3D) radiation transport hydrodynamics simulations, while acceleration and shock breakout data acquired with the established side-on system [5] are well reproduced by one-dimensional (1D) simulations. The experimental radiographs reveal the early-time imprinting of spatial modes (perturbation wavelength λ_{pert}) as short as $\lambda_{\text{pert}} = 8$ μm present in the irradiation profile, although the later-time evolution is found to be consistent with RT growth, dominated by longer λ_{pert}. Computational modeling reproduces the imprinting and RT phases with larger late-time amplitudes in longer λ_{pert} disturbances.

Planar C_8H_8 (parylene E, density $\rho = 1.07$ g/cm^3), and CH_2 (polypropylene, $\rho = 0.9$ g/cm^3) foils were driven with one beam of the VULCAN Nd:glass laser at irradiances from 4×10^{12} to 2×10^{13} W/cm^2. The laser provided 1–3 ns pulses at $\lambda = 0.527$ μm, with random phase plate (RPP) and/or induced spatial incoherence (ISI) smoothing [2] and $f/10$ main focusing optics. The temporal profile of the driving pulse was measured on a shot-to-shot basis, and consistently featured $\sim$500 ps linear rise to peak irradiance from $t = 0$, followed by a plateau and $\sim$500 ps fall, with the pulse length defined as the full width at half maximum. The rms surface uniformity of foils from the same samples were measured with an atomic force microscope to be $\sim$10 nm for the CH_2 sample, and $\sim$50 nm for the C_8H_8 sample. The laser energy was recorded on a shot-to-shot basis with absorbing glass calorimeters, while the irradiance profile incident on the foils was characterized on separate shots by imaging the focal spot at high magnification ($100\times$) directly onto film with a microscope objective. This provided a time-integrated measure of the (static) RPP irradiation nonuniformity for comparison with the induced target modulation and the input profile for the hydrocode runs. The RPP generated a sinc^2 envelope with $\sim$1.1 mm between first minima and $\sim$10 μm speckle superimposed.

Face-on radiography (at 18° to the target normal) was performed by imaging transmitted XUV radiation from a 550 μm gold backlighter target irradiated with $\lambda = 0.527$ μm light at $\sim 5 \times 10^{12}$ W/cm^{-2} for 1 ns (C_8H_8 case) or 2 ns (CH_2 case) with a temporal pulse shape as described above. The backlighter pulse was timed to be coincident with the drive pulse in each case. The transmitted radiation was imaged with a spherical-section multilayer mirror reflecting a narrow band ($\Delta E \sim 5$ eV) around 250 eV. For 250 eV photons, the cold C_8H_8 target has an optical depth of 2.05, which falls during

acceleration to 1.91 at 850 ps. The cold and in-flight values for the CH_2 target are 1.82 and 1.70 at 720 ps. The in-flight values are taken from simulations.

Multiple, temporally separated images at 69× magnification were recorded on each shot by a gated framing camera with ~120 ps temporal resolution. The spatial resolution was measured to be <3 μm by imagining a fine copper mesh, backlit with the XUV source. The modulation transfer function (MTF) of the system was similarly characterized and used to deconvolve the experimental data. The MTF was found to be above 0.75 for all $k < 8$, where k is the wave number in units of cycles per 64 μm, a convention adopted throughout this document. A similar system was used at 90° on separate shots on record side-on streak images of the target trajectory with a temporal resolution of 250 ps [5]. Figure 1 shows the experimental configuration [6].

The experimental observable is modulation in optical depth (δ) through the sample, $\delta = \langle -\ln I \rangle = \langle \int \rho \kappa_\nu dx \rangle$, where ρ is the material density, κ_ν is the material opacity at the probe frequency ν, the integral is performed over the line of sight, and $\langle\,\rangle$ denote the rms nonuniformity of the enclosed quantity. As described above, ν lies in the XUV range, to provide sufficient sensitivity and resolution, and hence κ is dependent on the material temperature T and mass density ρ. Accurate modeling of the experiment must therefore include detailed opacity predictions in order that δ can be recreated computationally and compared directly with the experimental data. This is the approach adopted here, where predictions of opacity codes are looked up at each point in the simulations to recreate δ self-consistently.

Computational simulations were performed in 1D, 2D, and 3D using the FAST laser matter interaction model [7]. All simulations employed a Eulerian finite-volume difference scheme. RAD3D_CM, the 3D code used in this study, is a direct extension of FAST3D_CM [8] that includes radiation transport [9]. In the FAST model, laser energy is deposited by inverse bremsstrahlung with a dump at the critical surface and transported by classical Spitzer-Härm electron thermal conduction. A model tabulated [10] equation of state (EOS) is employed. Two sets of tabulated opacities were used, generated by the codes STA (super transition array) [11] and IMP (ionized material package) [12], with the opacity of cold material [13] used for $T <$ 1 eV. Differences between runs using each of the tables for otherwise identical conditions were negligible, and in the lower intensity regimes ($I < 1 \times 10^{13}$ W/cm^2), values of δ were also very similar to those generated in the absence of radiation transport. STA, IMP, and the EOS module assume local thermodynamic equilibrium (LTE).

All simulations employ planar, Cartesian geometry, and for multidimensional cases the ablation front and the RT spikes develop in regions where the cell size along the laser propagation axis x is within the range $0.3 \leq \Delta x \leq 0.75$ μm. Transverse cell sizes Δy and for 3D, Δz, were fixed at 0.5 μm. Outflow boundary conditions are imposed for x, with periodic boundary conditions for y and z.

Side-on streak data were compared with the codes by generating transmission profiles and comparing the trajectories of the 50% transmission contours for the front and rear target surfaces. Figure 2 shows these trajectories for a 7.3 μm C_8H_8 foil irradiated at $8.0 \pm 0.8 \times 10^{12}$ W/cm^2 for 3 ns. Also plotted are the results of a 1D simulation. The foil was ~1.2 mm deep in the line of sight, slightly larger than the RPP focal spot and not perfectly flat, so front side data are shown until 500 ps, at which point the undriven foil obscured the line of sight until 1 ns when the rear side emerged from shadow. The mean acceleration during the first 1.3 ns is 3.2×10^{15} cm/s^2.

For multidimensional simulations, the seed for the multimode RT perturbations is provided by spatial nonuniformities in the incident laser. 2D simulations were performed with various definitions for the driving profile with best agreement with 3D simulations and the experimental data found for a lineout taken directly from the measured 2D intensity profile and possessing the same rms nonuniformity as the full set (hereafter referred to as the "rms equivalent" lineout). Although this lineout did not exactly recreate the full spectral content of the 2D profile, it retained a representative cross section of the features therein. Poorer agreement was found for runs performed using generated profiles with the same modal structure as the full 2D profile, since the rms uniformity could not be matched simultaneously. Simulations in 3D were performed by using the experimentally acquired intensity profile passed through a 2D Fourier filter with a low-pass hard cut at $k = 8$ to ensure good conditioning for the periodic boundaries. The spectral information for $k > 8$ was of low amplitude (<10%) and concerned with the shape of spikes in the drive profile, rather than relating to independent spatial structures, and since the computational mesh was designed with transverse cells of 0.5 μm

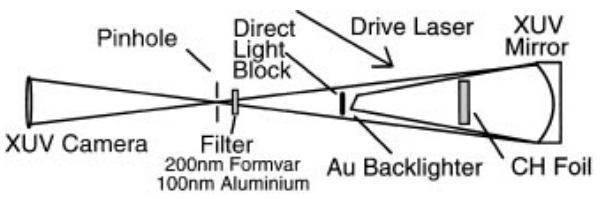

FIG. 1. Experimental configuration for XUV radiography.

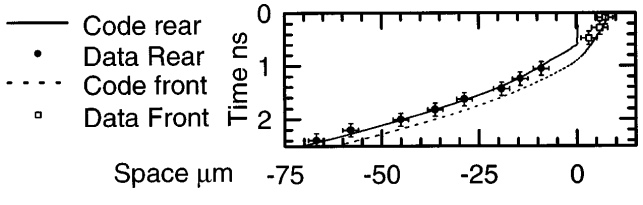

FIG. 2. Comparison of 50% transmission contours from side-on radiographic data with 1D FAST predictions.

to resolve the structure of $k \leq 8$, the filter did not significantly affect the simulation evolution. Direct comparison between codes and data was achieved by configuring the codes to generate $\delta(y, z)$ profiles. Figure 3 shows these from XUV radiographs (b, c, d) of a 7.3 μm C_8H_8 foil during irradiation at $I = 4.2 \pm 0.4 \times 10^{12}$ W/cm^2. A typical measured irradiance profile is shown in (a). The accompanying lineout reveals the ~10 μm speckle, measured to have a rms nonuniformity of 75%. The side-on data show that the distance traveled during the experiment was less than 100 μm, small compared to the spot size, hence "edge effects" are negligible. Similar face-on results were also obtained for targets overcoated with 1000 Å of Al to ensure that no light directly reached the interior of the target.

For the conditions prevailing in Figs. 3–6, shock breakout is predicted to occur at 650 ± 50 ps, with the temporal spread due to the nonuniform velocity along the shock front. Hence, Fig. 3(b) represents the extent of imprinting just prior to shock breakout, (c) the state of the target after the initial acceleration and RT growth of the imprinted nonuniformity, and (d) after burnthrough. Figures 3(e)–3(g) show frames from a RAD3D_CM 3D simulation using the typical irradiance profile shown in Fig. 3(a). The irradiance profile (a) correlates well with the early-time contrast plots but bears less relation to the later-time data and simulation results, where the lower-k modes can be seen to dominate.

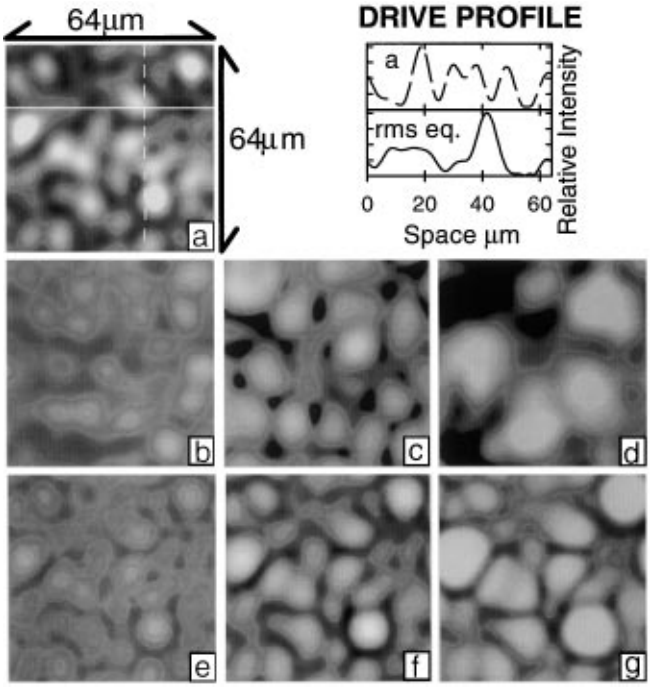

FIG. 3. Typical irradiance profile (dotted lineout) and rms equivalent (solid lineout) (a) and XUV radiographs at (b) 560 ps, (c) 860 ps, and (d) 2135 ps of a 7.3 μm C_8H_8 foil irradiated with RPP smoothing at $I \sim 4.2 \times 10^{12}$ W/cm^2. Frames (a)–(d) were passed through a low-pass Fourier filter with a hard cut at $k = 8$. Also shown are optical depth profiles generated by RAD3D_CM at (e) 560 ps, (f) 860 ps, and (g) 1450 ps for the same conditions.

Figure 4 shows Fourier spectra of the drive profile, and optical depth profiles measured experimentally and predicted by RAD3D_CM. This illustrates the trend to dominance of the longer modes. Between 560 and 860 ps computationally, the mean amplitude of modes $k = \sqrt{2}$ to 4 increases 130%, while for $k = 4$ to 6, the mean increases by only 90%. This compares with increases of 150% and 80%, respectively, for the data. For the 2D and 3D simulations, $k_{2D} \approx 2$ and $k_{3D} = (k_y^2 + k_z^2)^{1/2} \approx 2$ to 3, respectively, emerge as the dominant modes as the target approaches burnthrough (c), consistent with the 2135 ps data (d).

The δ predicted by the code and measured from the data is reproduced in Fig. 5, where (a) is the C_8H_8 case, and (b) is for a shot with an 8 μm CH_2 foil irradiated at $1.8 \pm 0.6 \times 10^{13}$ W/cm^2. In Fig. 5(a), results from 3D and the rms equivalent 2D simulations are presented. At these intensities, the effect of radiation is a slightly lower δ (within 5% through 1250 ps), a result of the enhanced heating and longer scale lengths produced by the longer mean free path components of the radiative self-emission. This effect was more marked for the higher irradiance CH_2 case.

Foils driven with temporally incoherent irradiation (RPP + 5 × 5 étalon ISI smoothing with bandwidth $\delta\omega/\omega = 0.1\%$) exhibited less imprint, e.g., $\delta = 0.36 \pm 0.05$ at 2.4 ns for 3 μm C_8H_8 irradiated at $8.3 \pm 0.8 \times 10^{12}$ W/cm^2. With this smoother time-averaged drive profile, dominance of longer modes was not observed despite the higher acceleration.

We define the "imprint phase" as the period before the return of the first rarefaction wave to the ablation surface after shock breakout. After this time (t_R), the targets accelerate uniformly (to within 10% for C_8H_8 and 8% for CH_2) through the "RT phase" until thinning of the target to the point where the axial peak density in a bubble falls below 0.4 g/cm^3 (at $t = t_{th}$) leads to burnthrough.

By means of 2D simulation we tested the importance of two potential contributors to the imprinting process. By inhibiting lateral material flow in the simulation, different rates of ablation became the only source of variation in areal density. Within 100 ps these solutions began to

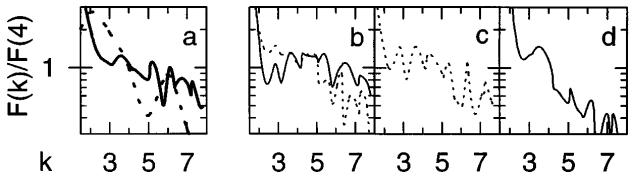

FIG. 4. Fourier spectra of (a) RPP profile (solid curve) and rms equivalent lineout used for 2D simulations (dotted curve); (b) experimental data (solid curve) and RAD3D_CM prediction (dotted curve) at $t = 860$ ps; (c) RAD3D_CM prediction at 1450 ps and (d) experimental data at 2135 ps. The curves are scaled to the amplitude at $k = 4$ for consistency.

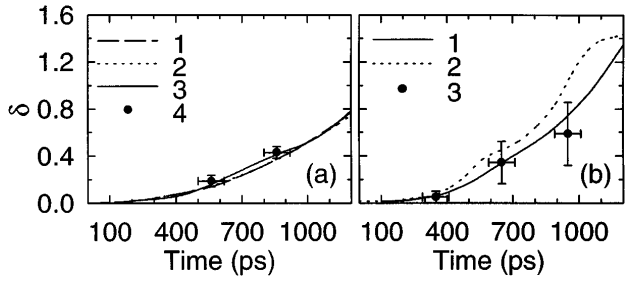

FIG. 5. Comparison of δ for 2D and 3D simulations and experimental data for (a) C_8H_8 and (b) CH_2 targets, irradiated at $I \sim 4.2 \times 10^{12}$ W/cm^2 and $I \sim 1.8 \times 10^{13}$ W/cm^2, respectively. (a4) Experimental datapoints; (a1,a2) 2D rms equivalent case, (1) without and (2) with radiation transport (obscured by other curves); (a3) 3D case. (b3) Experimental data points; (b1,b2) 2D case with radiation transport. Laser intensity: (1) 1.3×10^{13} W/cm^2; (2) 2.3×10^{13} W/cm^2 to cover the experimental error in measured irradiance. The experimentally measured temporal pulse shape was used in all simulations.

diverge dramatically from those where lateral flow was permitted, suggesting that hydrodynamic flow dominates over the nonconstant ablation profile.

Simulations were also performed where drive nonuniformity was removed after (a) 100, (b) 250, and (c) 500 ps of run time. The runs (c) generated growth that was within 10% of that obtained with permanently modulated irradiation, indicating that the drive nonuniformity had decoupled from the ablation surface by 500 ps. The RT phase began later than 500 ps ($t_R \approx 1$ ns), and hence the system's evolution after t_R and before t_{th} is dominated by residual (inertial) flow from the imprint phase and the RT instability.

In Fig. 6, the temporal evolution of areal density mode amplitudes from the 3D simulation of the C_8H_8 case is presented. The wave numbers are divided into "long" ($\sqrt{2} \le k < 4$) and "short" ($4 \le k \le 6$) groups, with slightly higher growth observed for the short modes prior to shock breakout. At this point the short modes saturate while the long modes continue to grow, dominating the evolution through the ensuing ablative acceleration. Using techniques described in [8], we observe that the

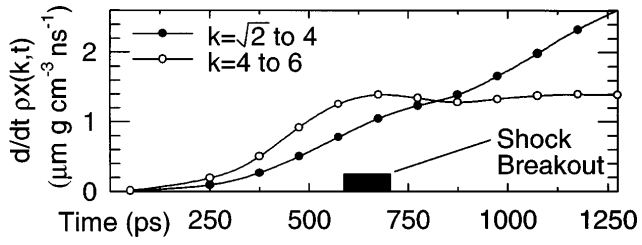

FIG. 6. Evolution of long ($\sqrt{2} \le k_{3D} < 4$) and short ($4 \le k_{3D} \le 6$) modes in the target's areal density profile (3D simulation, C_8H_8 case). Plotted is the time derivative of the mean Fourier amplitude in each of the ranges. The shorter wavelengths saturate during shock breakout and exhibit less RT growth during the subsequent acceleration.

very short modes ($k > 6$) saturate prior to shock breakout, then later during the RT phase exhibit a burst of growth consistent with higher-order mode coupling and shape effects. The reduced growth for shorter modes may be due to multimode feeding effects similar to the nonlinear interactions that provide an inverse cascade in 2D hydrodynamic turbulence [14]. Extended analysis of the multimode behavior and concurrent RT growth will be given in a forthcoming paper.

In summary, we have reported on measurements of in-flight target nonuniformity seeded by imprinting of temporally coherent and incoherent laser irradiation. Predictions of 2D and 3D radiation transport hydrodynamic simulations have been compared with the experimental measurements. The 2D case agrees with the 3D case and experimental data, but only for a particular choice of driving irradiance profile. In both experiment and simulation, peak growth in the modal target perturbation spectrum shifts from shorter to longer wavelengths with time. A period of RT growth is isolated, after which 20 to 30 μm modes dominate. The results suggest that hydrodynamic flow is the dominant imprint mechanism.

We acknowledge helpful discussions with Dr. Steven Rose (RAL), Dr. Matt Desselberger (IC), Dr. Colin Smith, and John Edwards (AWE), Stephen Obenschain and Stephen Bodner (NRL). We are grateful to Dr. Steven Rose and Dr. David Garren (SAIC, NRL) for generating the opacity tables used in the calculations reported here, to the staff of the Central Laser Facility for their help and support during the experiments, and to Dr. Brian Evans of Reading University for supplying the XUV mirrors. Simulations for this study were performed on the CEWES/DOD-HPC and the NRL CM-5. This work was partially supported by EPSRC and MOD grants and by the U.S. Department of Energy.

[1] M. H. Emery *et al.*, Phys. Fluids B **3**, 2640 (1992).
[2] Y. Kato and K. Mima, Phys. Rev. Lett. **53**, 1057 (1984); R. H. Lehmberg and S. P. Obenschain, Opt. Commun. **46**, 27 (1983); S. Skupsky *et al.*, J. Appl. Phys. **66**, 3456 (1989).
[3] M. Desselberger *et al.*, Phys. Rev. Lett. **68**, 1539 (1992).
[4] J. D. Kilkenny *et al.*, Phys. Plasmas **1**, 1379 (1994).
[5] J. Edwards *et al.*, Phys. Rev. Lett. **71**, 3477 (1993).
[6] M. Desselberger *et al.*, Appl. Opt. **30**, 2285 (1991); O. Willi *et al.*, Rev. Sci. Instrum. **63**, 4818 (1992).
[7] M. H. Emery, J. H. Gardner, and J. P. Boris, Appl. Phys. Lett. **41**, 808 (1982).
[8] J. P. Dahlburg *et al.*, Phys. Plasmas **2**, 2453 (1995).
[9] J. H. Gardner *et al.*, Bull. Am. Phys. Soc. **33**, 2110 (1988).
[10] C. R. DeVore *et al.*, Laser Part. Beams **2**, 227 (1984).
[11] A. Bar-Shalom *et al.*, Phys. Rev. A **40**, 3183 (1989).
[12] S. Rose, J. Phys. B **25**, 1667 (1992).
[13] B. L. Henke, E. M. Gullikson, and J. C. Davis, At. Data Nucl. Data Tables **54**, No. 2 (1993).
[14] D. E. Fyfe, D. C. Montgomery, and G. Joyce, J. Plasma Phys. **17**, 369 (1977).